

# FLAP EFFICIENCY ANALYSIS FOR THE SAGITTA DIAMOND WING DEMONSTRATOR CONFIGURATION

A. Hövelmann, S. Pfnür, C. Breitsamter

Institute of Aerodynamics and Fluid Mechanics, Technische Universität München  
Boltzmannstr. 15, 85748 Garching bei München, Germany

## Abstract

The efficiency of deflected midboard flaps is investigated on a diamond wing shape unmanned aerial vehicle, the SAGITTA demonstrator configuration. The Reynolds-Averaged Navier-Stokes equations are applied to compute numerical results for a variety of flight conditions with varying angle of attack, sideslip angle and midboard flap deflection. Low speed wind tunnel conditions are regarded in order to compare the results to existing experimental data. The focus is particularly laid on the analysis of the aerodynamic coefficients and derivatives in both the longitudinal and the lateral motion. Occurring flow phenomena are motivated and discussed by flow field illustrations that are available from the numerical computations. At small to moderate angles of attack, the overall flow field is dominated by attached flow, which is associated with linear flap characteristics. With increasing angle of attack and additional sideslip angle, the leading-edge vortex originating from the inboard sharp leading-edge and the wing tip separation region affect the midboard flap efficiency in some extent. The roll control effectiveness is mostly ensured, but non-linear coupling effects become obvious, which are analyzed and discussed.

## NOMENCLATURE

$b$	Wing span, [m]	$S_{Ref}$	Wing reference area, [m <sup>2</sup> ]
$C_D$	Drag coefficient, $C_D = \frac{D}{q_\infty \cdot S_{Ref}}$	$s$	Wing half span, [m]
$C_L$	Lift coefficient, $C_L = \frac{L}{q_\infty \cdot S_{Ref}}$	$U_\infty$	Free stream velocity, [m/s]
$C_Y$	Side force coefficient, $C_Y = \frac{Y}{q_\infty \cdot S_{Ref}}$	$u$	Axial velocity, [m/s]
$C_{mx}$	Rolling moment coefficient, $C_{mx} = \frac{M_x}{q_\infty \cdot S_{Ref} \cdot s}$	$x, y, z$	Cartesian coordinates, [m]
$C_{my}$	Pitching moment coefficient, $C_{my} = \frac{M_y}{q_\infty \cdot S_{Ref} \cdot l_\mu}$	$Y$	Side force (wind-axis COS), [N]
$C_{mz}$	Yawing moment coefficient, $C_{mz} = \frac{M_z}{q_\infty \cdot S_{Ref} \cdot s}$	$y^+$	Dimensionless wall distance
$c$	Wing chord, [m]	$\alpha$	Angle of attack, [deg]
$c_p$	Pressure coefficient, $c_p = \frac{p - p_\infty}{q_\infty}$	$\beta$	Angle of sideslip, [deg]
$D$	Drag (wind-axis COS), [N]	$\Lambda$	Wing aspect ratio
$g$	Prism Layer Stretching Factor	$\lambda$	Wing taper ratio
$h_1$	Initial Prism Layer Thickness, [m]	$\xi$	Midboard flap deflection angle, [deg], $\xi = \frac{\xi_R - \xi_L}{2}$
$L$	Lift (wind-axis COS), [N]	$\rho_\infty$	Free stream density, [kg/m <sup>3</sup> ]
$l_\mu$	Mean aerodynamic chord, [m]	$\varphi$	Wing sweep angle, [deg]
$M_x$	Rolling moment (body-fixed COS), [Nm]	<b>Subscripts</b>	
$M_y$	Pitching moment (body-fixed COS), [Nm]	$L$	Left
$M_z$	Yawing moment (body-fixed COS), [Nm]	$LE$	Leading-edge
$Ma$	Mach number	$MRP$	Moment reference point
$p$	Static pressure, [N/m <sup>2</sup> ]	$R$	Right
$p_\infty$	Free stream static pressure, [N/m <sup>2</sup> ]	$r$	Root chord
$q_\infty$	Free stream dynamic pressure, [N/m <sup>2</sup> ], $q_\infty = \frac{\rho_\infty \cdot U_\infty^2}{2}$	$TE$	Trailing-edge
$Re$	Reynolds number	$t$	Tip chord
$r_N$	Leading-edge radius, [m]		

## 1 INTRODUCTION

Well designed control devices are in general a key factor in aircraft design to efficiently fly and control the air vehicle. Especially for agile configurations with highly swept low aspect ratio wings featuring delta, lambda or diamond planforms, this aspect becomes essential, since it mainly determines the maneuverability and agility of the aircraft [1]. Lever arms available for the generation of control moments are typically small. At higher angles of attack, the flow field is often dominated by separated flow, which can lead to non-linear characteristics and decreased control efficiency. In the design and development of future unmanned aerial vehicles (UAV), the above mentioned type of wing configuration is often considered [2]. In order to reduce its radar signature, they are commonly regarded as tail-less flying wing configurations, which drastically reduces the directional stability [3, 4]. Additionally, coupling effects between different control devices arise in many cases [5], which mainly affects its efficiency and leads both to decreased maneuverability and agility. Thus, the optimization of the control devices is of primary interest in particular for this type of aircraft configuration, as their efficiency is essential for the performance and application range of the aircraft.

In this context, the Institute of Aerodynamics and Fluid Mechanics at Technische Universität München (TUM-AER) investigates the aerodynamic characteristics of the SAGITTA diamond wing demonstrator configuration, Figure 1. The analyses refer to a research program of AIRBUS Defence & Space, which follows an Open Innovation approach [6]. It aims on the design and development of a tail-less flying wing demonstrator that is jointly built by several partners from German universities and research institutes. The diamond wing shape UAV demonstrator configuration features a root chord length of  $c_r = 3 \text{ m}$  and a full wing span

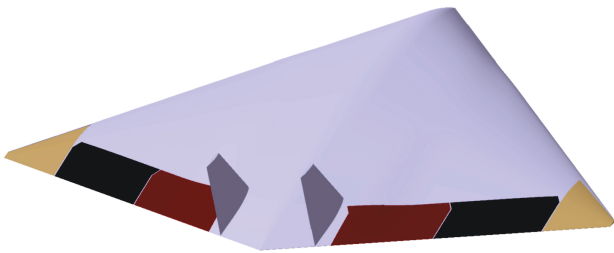


Figure 1: SAGITTA diamond wing demonstrator configuration with main control devices and double V/T.

of  $b = 3.088 \text{ m}$ , resulting in a maximum take off weight of  $m_{MTOW} = 144 \text{ kg}$ . Three main control devices are defined at the wing trailing-edge for pitch, roll and yaw control, Figure 1. For the first flight campaign of the SAGITTA demonstrator configuration scheduled in 2015, a double vertical tail (V/T) is added to the configuration, accounting thus for increased lateral directional stability.

## 2 RECENT RESEARCH ACTIVITIES

The investigations on the SAGITTA diamond wing demonstrator configuration are performed both experimentally and numerically at TUM-AER. On the one hand, a 1:3-scaled wind tunnel (W/T) model featuring a root chord length of  $c_r = 1.0 \text{ m}$  has been built. Based on a NACA64A012 airfoil with 12% relative thickness, the configuration is equipped with varying leading-edge contours along the wing half span. At the inner 20%, it features a sharp leading-edge contour, whereas a rounded leading-edge contour is present elsewhere in the outer wing sections ( $r_N/c = 0.994\%$ ). Details on the W/T model can be noticed from Figure 2 and Table 1.

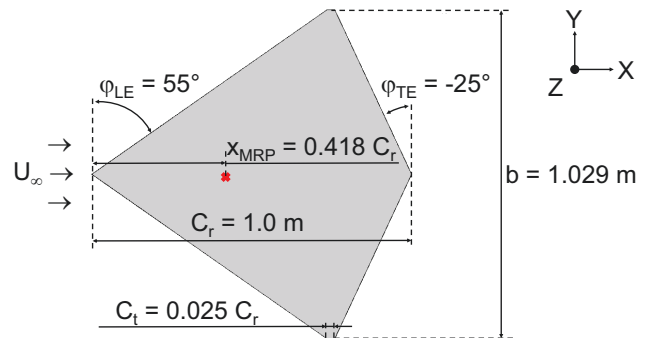


Figure 2: Wing planform of the SAGITTA diamond wing demonstrator W/T configuration, top view xy plane.

$c_r$ [m]	$c_t$ [m]	$\lambda$ [—]	$\phi_{LE}$ [°]	$\phi_{TE}$ [°]
1.0	0.025	0.025	55	-25

$b$ [m]	$S_{Ref}$ [m <sup>2</sup> ]	$\Lambda$ [—]	$l_\mu$ [m]	$x_{MRP}$ [m]
1.029	0.528	2.001	0.667	0.418

Table 1: Wing planform parameters of the SAGITTA diamond wing demonstrator W/T configuration.

The control devices for pitch, roll and yaw control are integrated to the W/T model and can be adjusted continuously by electrically powered model servos. The aerodynamic forces and moments are measured by an external balance, as the W/T model is rear sting mounted in the test section, Figure 3. Extensive experimental investigations have been undertaken so far, from which an aerodynamic data module (ADM) has been derived [7]. In addition to the analysis of the clean wing configuration with and without V/T, numerous variations of different control device deflections and configurations with deployed landing gears or a camera gimbal have been measured. The ADM, which provides thus a broad experimental data base, has ever since widely been used within the design process of the SAGITTA demonstrator configuration [8, 9].

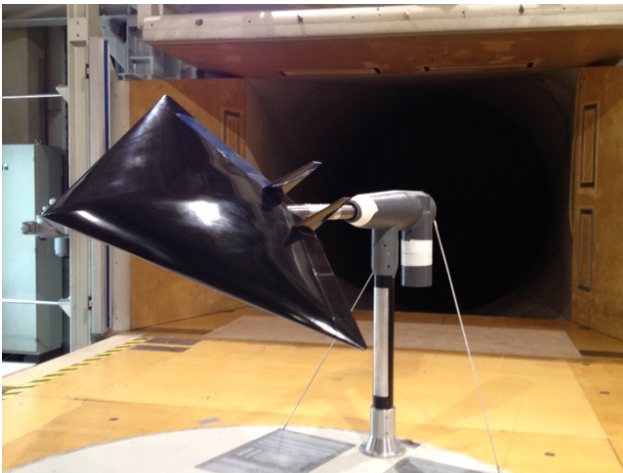


Figure 3: SAGITTA diamond wing demonstrator W/T configuration within the test section.

On the other hand, comprehensive numerical analyses have been undertaken. Initial CFD (Computational Fluid Dynamics) computations of both the clean wing configuration with and without V/T and selected cases with deflected inboard and midboard (I/B and M/B, respectively) flaps have been conducted via steady-state RANS (Reynolds-Averaged Navier-Stokes) computations. First results including W/T results and CFD investigations of the clean wing configuration have already been published [7]. The basic aerodynamic characteristics of the SAGITTA diamond wing demonstrator configuration have thus been presented.

In this publication, the focus is now set to a flap efficiency analysis of the M/B control devices. For the analysis, the first flight configuration including V/T is regarded (W/T size). The M/B flaps are deflected for all considered flight condi-

tions asymmetrically on both wing half surfaces. The clean wing configuration serves as baseline case. The presented results comprise numerical and experimental investigations, which are compared in detail to each other. For the CFD results, current computations on refined meshes are introduced, thus accounting for more detailed flow field phenomena. In addition to the longitudinal motion, the lateral motion is regarded as well, for which flow conditions with sideslip angles are taken into consideration.

### 3 NUMERICAL APPROACH

#### 3.1 Mesh Generation

The hybrid meshes of the presented numerical computations are generated with the commercial mesh generation software CENTAUR<sup>1</sup>. Based on an unstructured surface mesh consisting of triangles and quadrilaterals, prismatic and hexahedral elements are used close to the wing surface in the boundary layer region. Elsewhere in the computational domain, tetrahedral and pyramidal elements are used. The farfield boundaries are located 20 wing half span lengths away from the diamond wing nose. Since the present analysis requires the mesh generation of several asymmetric M/B flap deflections on both wing half surfaces, the applied meshing philosophy is as follows: Within CENTAUR, the right wing half is regarded exclusively. Moreover, the M/B flap region is limited by an interface box, which is meshed in a modular way. At first, the basic mesh of the right wing half including one M/B flap deflection and the tetrahedral farfield is completely built, Figure 4a. Next, the M/B flap geometry is altered and the new mesh is only built within the interface box. The existing mesh around the box serves as reference for the mesh node links, Figure 4b. Following, the basic mesh including the main wing surface and the tetrahedral farfield is only built once, while the box including the M/B flap region is meshed for every M/B flap deflection and the clean wing configuration. The full wing mesh required for the numerical computations is finally obtained by adequate tools for mirroring and adding the appropriate mesh components, which are available due to the modular mesh generation process, Figure 4c. Following this approach, a symmetric mesh except for the modular boxes can be ensured, which is of great importance for the numerical computations, in particular for the longitudinal motion.

<sup>1</sup><https://www.centaurosoft.com>, retrieved August 2014

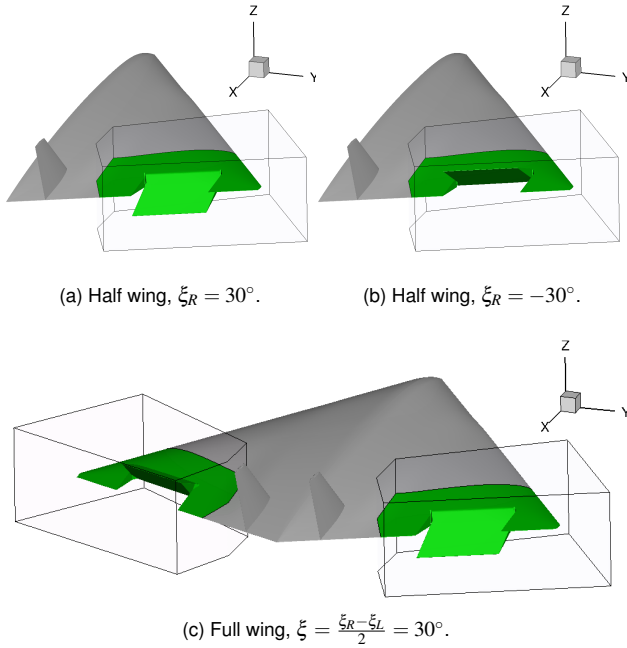


Figure 4: Modular mesh approach including interface boxes for the deflected M/B flaps.

In line with former numerical investigations of related low aspect ratio, vortex dominated wing configurations [2, 5, 10], the surface mesh is considerably refined close to the wing leading-edge. In order to accurately approximate the boundary layer flow in normal direction to the wing surface, the prism mesh contains 38 prism layers. Based on a target maximum  $y^+$  value of  $y^+ = 1$ , the viscous sublayer is therefore resolved by an initial layer thickness of  $h_1 \approx 0.004 \text{ mm}$ . For the subsequent 29 prism layers, a stretching factor of  $g = 1.235$  is applied to the mesh generation process of all considered configurations. The final eight prism layers exhibit a constant cell height. In the proximity of the wing sur-

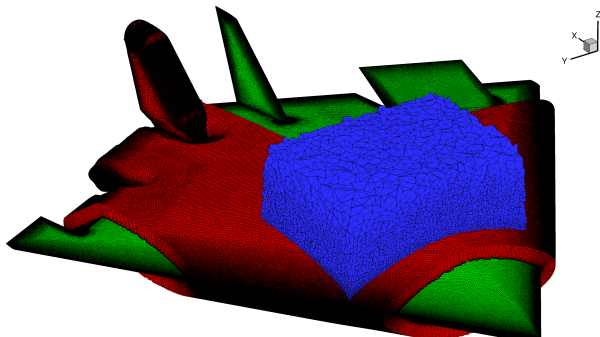


Figure 5: Hybrid mesh of the SAGITTA diamond wing demonstrator configuration with deflected M/B flaps and double V/T.

face, the tetrahedral mesh is additionally refined. Thereby, both the vortex structures originating from the leading-edge and the tip vortices of wing tip and M/B flaps dominating the wake flow field can be appropriately captured. In Figure 5, a break-up of one resulting mesh is presented by example. It depicts the configuration with maximum deflection of the M/B flaps. Table 2 summarizes the final mesh sizes of the seven analyzed configurations. As it can be noticed, the absolute number of mesh nodes differs only slightly between the configurations with deflected M/B flaps. Compared to the clean wing configuration, however, considerably more mesh nodes are required.

Configuration	No. of Nodes	No. of Elements
$\xi = 30^\circ$	$30.10 \cdot 10^6$	$81.79 \cdot 10^6$
$\xi = 20^\circ$	$29.98 \cdot 10^6$	$81.79 \cdot 10^6$
$\xi = 10^\circ$	$29.82 \cdot 10^6$	$81.80 \cdot 10^6$
$\xi = 0^\circ$	$25.80 \cdot 10^6$	$71.23 \cdot 10^6$
$\xi = -10^\circ$	$29.82 \cdot 10^6$	$81.80 \cdot 10^6$
$\xi = -20^\circ$	$29.98 \cdot 10^6$	$81.79 \cdot 10^6$
$\xi = -30^\circ$	$30.10 \cdot 10^6$	$81.79 \cdot 10^6$

Table 2: Mesh size of the considered configurations.

### 3.2 Computational Fluid Dynamics Solver

The numerical investigations performed for this analysis are computed with the TAU-Code, a CFD solver developed at the DLR (German Aerospace Center) Institute of Aerodynamics and Flow Technology [11]. It solves the three-dimensional compressible steady or unsteady Reynolds-Averaged Navier-Stokes ((U)RANS) equations on hybrid meshes. Moreover, it is developed for optimized parallel efficiency on high-performance computers. The DLR TAU-Code uses a finite volume scheme and is based on a dual grid approach [12]. This implies the generation of a secondary grid during the preprocessing, which is computed according to the cell vertex grid metric from the initial (primary) grid provided by the mesh generation process. The preprocessor module furthermore generates the additional grids required for multigrid computations. The solver module of the DLR TAU-Code performs the flow computations. For finite volume discretization, several upwind and central schemes can be applied. The temporal discretization (local/dual/global time stepping) is dependent on steady-state or time-accurate computations. Both explicit and im-



implicit schemes are available, which are used in combination with the multigrid technique for convergence acceleration. If turbulent flows are considered, a variety of one- and two-equation models such as Spalart-Allmaras (SA) or  $k - \omega$  turbulence models as well as different kinds of Reynolds stress models (RSM) can be applied [11].

### 3.3 Test Conditions and Numerical Setup

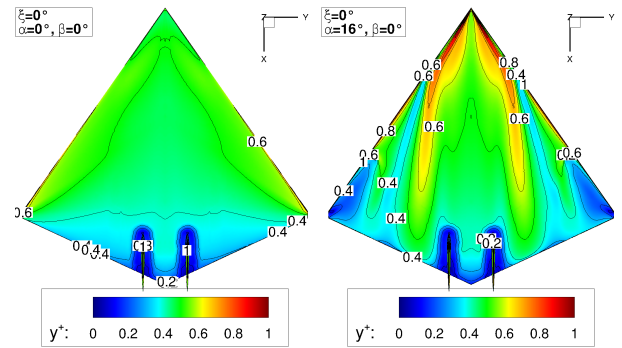
In order to compare the numerical and experimental results most efficiently, the low speed W/T conditions used for the experimental investigations are considered as well for the conducted CFD computations that are run fully turbulent. A free stream Mach number of  $Ma = 0.12$  and a Reynolds number of  $Re = 1.7 \cdot 10^6$  based on the mean aerodynamic chord of  $l_\mu = 0.667 \text{ m}$  are thus applied. The moment reference point for pitching and yawing moment calculation is set to the geometrical neutral point of the SAGITTA diamond wing demonstrator W/T configuration as introduced in Figure 2, which results in  $x_{MRP} = 0.418 \text{ m}$  aft of the diamond wing nose. The angle of attack varies within the CFD computations between  $\alpha = 0^\circ$  and  $\alpha = 16^\circ$ . The maximum regarded angle of sideslip of the present analysis reads  $\beta = 8^\circ$ . The computations have been run in parallel mode on 544 cores for the clean wing configuration and 624 cores for the configurations with deflected M/B flaps at the GCS Supercomputer SuperMUC at Leibniz Supercomputing Centre (LRZ)<sup>2</sup>.

For the present type of highly swept, vortex dominated aircraft configuration with both sharp and rounded leading-edges, numerous analyses have already shown the validity of the DLR TAU-Code including grid sensitivity studies and turbulence model analyses [1, 2, 5, 7, 10, 13–15]. For this reason, gained experiences of those investigations have been utilized for the numerical setup in the present analysis. Based on a cell vertex grid metric, a second-order central scheme introduced by Jameson is applied for spatial discretization [16]. The required artificial viscosity is added by a matrix valued coefficient (matrix dissipation scheme), for which the central difference scheme becomes closer to upwind biased methods [17]. For the discretization in time, an implicit Backward-Euler scheme with LUSGS algorithm is used [18]. The steady-state RANS computations are performed with local time stepping for the whole angle of attack

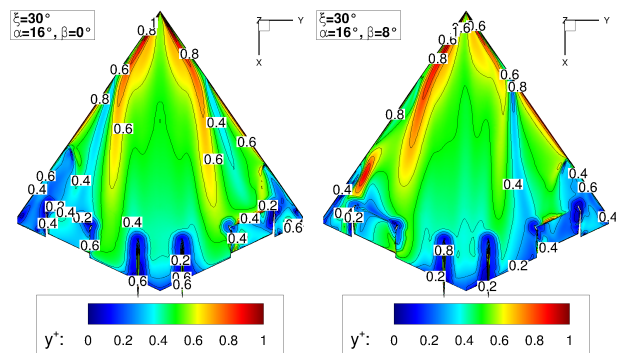
and sideslip angle range, applying 40000 iterations each per single run. In order to accelerate the convergence, a 3w multigrid cycle is furthermore used [19]. Turbulence is modelled within the present computations by the one-equation model of Spalart-Allmaras [20], but in a revised version (SA-Neg). The modifications particularly allow negative values of the transport turbulence quantities and lead to a more efficient solution of the equation without changing the aerodynamic solution [21].

## 4 RESULTS AND DISCUSSION

This section comprises the results of the numerical investigations carried out in the context of this analysis. Furthermore, the results are compared to existing W/T data of the SAGITTA demonstrator configuration. At the beginning, the overall computed  $y^+$  contour levels are shown by example for selected flight conditions, Figure 6. Thereby, the initial prism layer thickness chosen for the mesh generation process is reviewed. As it can be noticed, the target maximum  $y^+$  value of  $y^+ = 1$  suitable for the Spalart-Allmaras turbulence model is mostly undermatched. At higher angles of



(a) Clean wing configuration, effect of increased angle of attack.



(b) M/B flaps deflected, effect of increased sideslip angle.

Figure 6:  $y^+$  contour levels of selected flight conditions.

<sup>2</sup> <http://www.lrz.de/services/compute/supermuc/>, retrieved August 2014

attack, an increase of the  $y^+$  values is observed in the surface regions influenced by the leading-edge vortices, but the values do not exceed  $y^+ = 1$ , Figure 6a. For the configuration with deflected M/B flaps, the overall  $y^+$  contour levels are slightly affected in the proximity of the M/B control device, Figure 6b. However, the values remain in the same range as discussed for the clean wing configuration, even at higher angles of attack with present sideslip angle.

## 4.1 Clean Wing Configuration

### 4.1.1 Longitudinal Motion

The aerodynamic characteristics of the SAGITTA diamond wing demonstrator configuration are considered, incipient for the longitudinal motion. At first, the analysis is presented for the clean wing configuration without M/B flap deflection, so that the overall flow phenomena occurring at the diamond wing can be introduced and discussed. Figure 7 depicts the longitudinal aerodynamic coefficients for both the experimental (W/T) and the numerical (CFD) data set.

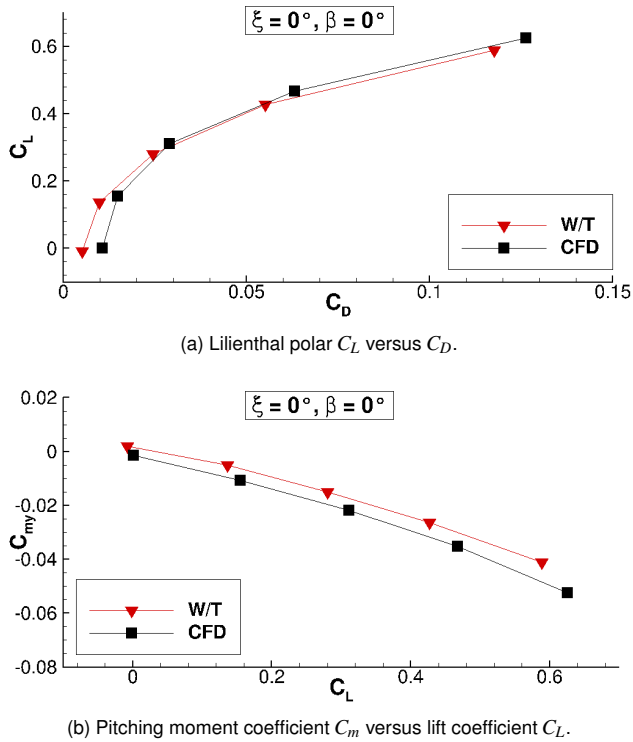


Figure 7: Longitudinal aerodynamic coefficients of the clean wing configuration at  $\beta = 0^\circ$ .

The Lilienthal polar in Figure 7a shows certain deviations between the two data sources. Compared to the numerical computations, considerably lower drag coefficients  $C_D$  are

observed in the W/T experiments, especially for the zero drag coefficient  $C_{D,0}$ . It can be explained, as all presented CFD computations are run fully turbulent, whereas the flow at the W/T model has not been forced to transition close to the wing leading-edge. The difference in the  $C_D$  values thus show that within the W/T tests, also laminar flow is present on the diamond wing surface. At higher lift coefficients and hence, at higher angles of attack, it is further noted that the CFD solution results in increased lift coefficient values compared to the W/T data. This fact is motivated again by different boundary layer characteristics, which influence the size of the emerging wing tip separation region, Figure 8.

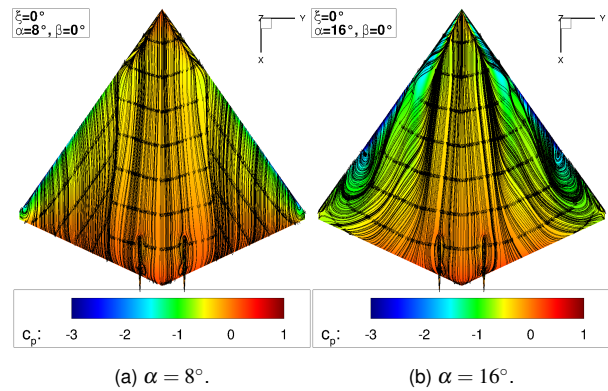


Figure 8: Surface streamlines of the clean wing configuration at  $\beta = 0^\circ$ .

With increasing angle of attack, the flow separates at the diamond wing tip, whereas the midboard region is still dominated by attached flow. Due to the rounded leading-edge contour and the thick airfoil, no vortex structure is formed in the outboard wing section, but a region of irregular flow with flow reversal, Figure 8 and Figure 9. For fully turbulent boundary layer conditions, the flow is less thread by separation than it is for laminar boundary layer flow. Following, the wing tip separation region is smaller within the CFD computations, leading to an increased region of attached flow. This region is dominant in the present case and leads thus to increased lift coefficients of the CFD runs in comparison to the W/T data.

In the inboard section of the SAGITTA diamond wing demonstrator configuration, the sharp leading-edge contour provokes the generation of a leading-edge vortex, which grows in size and intensity with increasing angle of attack, Figure 8. Due to the non-slender leading-edge sweep and the thick airfoil, however, the vortex is not of axial jet type,

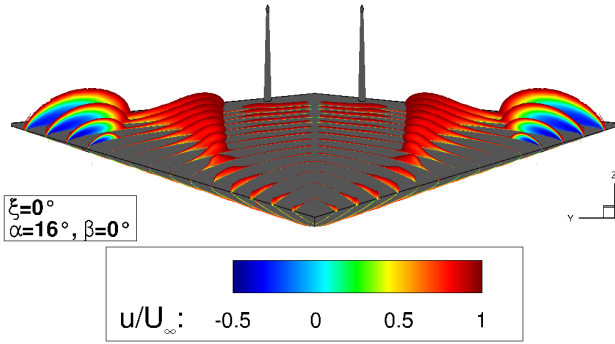


Figure 9: Axial velocity contour slices of the clean wing configuration at  $\alpha = 16^\circ$  and  $\beta = 0^\circ$ .

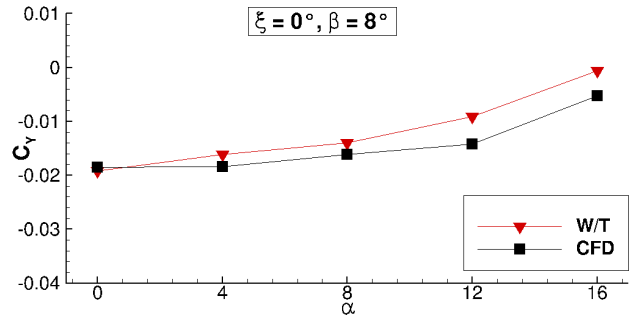
but the axial fluid transport within the vortex core is slightly retarded, Figure 9. Thereby, the leading-edge vortex does not play a major role for the integral aerodynamic coefficients, as they are dominated by the regions of attached and irregular separated flow originating from the rounded leading-edge contour.

In Figure 7b, the pitching moment characteristics are presented. In relation to the chosen moment reference point, the configuration is noted to be stable. The differences of the pitching moment coefficient values between the W/T experiments and the CFD computations are mainly related to the deviations of the lift coefficients as discussed above. With increasing angle of attack, the differences become slightly larger. For the present type of low aspect ratio wing configuration, deviations in the pitching moment characteristics are typical, as the prediction is known to be very sensitive both in CFD and in W/T investigations [2, 5].

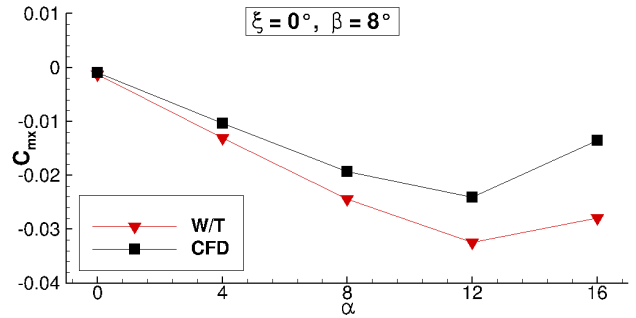
#### 4.1.2 Lateral Motion

Next, the effects of the sideslip angle on the lateral aerodynamic coefficients of the clean wing configuration are regarded. In Figure 10, the corresponding coefficients are shown at  $\beta = 8^\circ$ . The lateral aerodynamic coefficients  $C_Y$ ,  $C_{mx}$  and  $C_{mz}$  are mainly dominated by the effects originating from the double V/T, which is added for the first flight campaign to provide increased directional stability. At higher angles of attack, the rolling moment coefficient  $C_{mx}$  is additionally influenced by the flow separation characteristics.

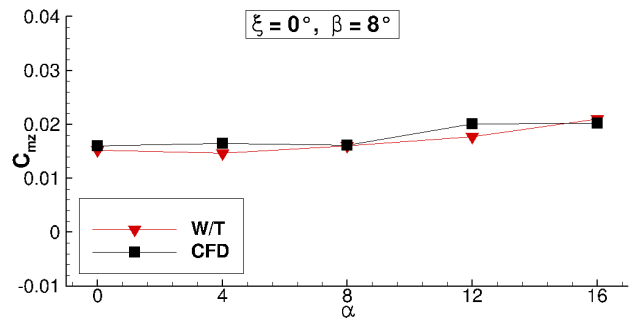
For the side force coefficient  $C_Y$ , small deviations are observed between both data sources, Figure 10a. The trend of the curves, however, is matched very well. With increasing angle of attack, the negative side force is decreased,



(a) Side force coefficient  $C_Y$ .



(b) Rolling moment coefficient  $C_{mx}$ .



(c) Yawing moment coefficient  $C_{mz}$ .

Figure 10: Lateral aerodynamic coefficients of the clean wing configuration versus angle of attack  $\alpha$  at  $\beta = 8^\circ$ .

since the inboard leading-edge vortex of the right wing half aligns the streamlines in chord-wise direction, Figure 11. Between  $\alpha = 12^\circ$  and  $\alpha = 16^\circ$ , the gradient of the curves increase even more, as the intensity of the leading-edge vortex increases and the wing tip separation region grows. The flow incipient to the V/T is thereby influenced more distinct, which results in even more decreased negative side force values and the small kink of the side force coefficient curves. Despite the sideslip angle of  $\beta = 8^\circ$ , almost no side force component is left at the angle of attack of  $\alpha = 16^\circ$ .

The yawing moment coefficient  $C_{mz}$  varies only slightly with increasing angle of attack and results in positive values, Figure 10c. Within the body-fixed coordinate system chosen for the moment coefficients, this leads to the known

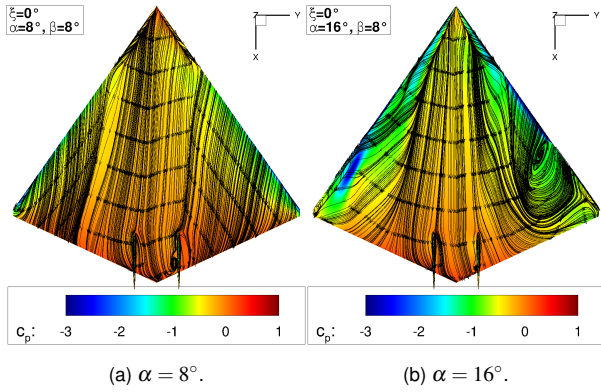


Figure 11: Surface streamlines of the clean wing configuration at  $\beta = 8^\circ$ .

weathercock stability. Both the W/T data and the CFD computations result in very similar values of  $C_{mz}$ , which are close to each other.

The analysis of the rolling moment coefficient  $C_{mx}$ , in contrast, requires more attention to the occurring flow phenomena discussed above, as the gradient of the resulting curves changes sign at higher angles of attack, Figure 10b. Up to the angle of attack of  $\alpha = 12^\circ$ , the rolling moment coefficient decreases almost linearly and results in negative values. This is caused by the moment around the x-axis generated at the double V/T, which leads to a counter-clockwise rotation of the wing with right wing tip up. In comparison to the W/T experiments, the values computed by CFD are less negative and show a certain deviation. At the angle of attack of  $\alpha = 16^\circ$  and the present sideslip angle, however, the intensity of the inboard leading-edge vortex and the size of the emerging separation region become such different on both wing half surfaces so that they influence the rolling mo-

ment characteristics more considerable. The effects originating from the V/T are now dominated by the mentioned flow phenomena. Due to the sideslip angle, the effective leading-edge sweep is decreased on the windward and increased on the leeward side of the diamond wing configuration. Thereby, the inboard leading-edge vortex becomes weaker on the windward and stronger on the leeward side of the diamond wing, Figure 12. The separation region of the outboard section becomes larger on the windward side, Figure 8b and Figure 11b. On the leeward side, in contrast, the region of irregular flow vanishes with present angle of sideslip and an additional outboard leading-edge vortex emerges, Figure 11b and Figure 12b. This vortex, originating from a rounded leading-edge contour, is of retarded type as well, but does not show any flow reversal in the vortex core axis, Figure 13. As a result, the overall lift is decreased on the windward and increased on the leeward side, which provokes a clockwise rolling moment. This counteraction is finally noted in the integral rolling moment characteristics by

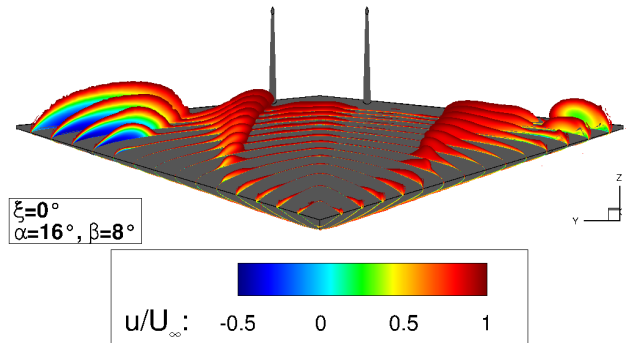


Figure 13: Axial velocity contour slices of the clean wing configuration at  $\alpha = 16^\circ$  and  $\beta = 8^\circ$ .

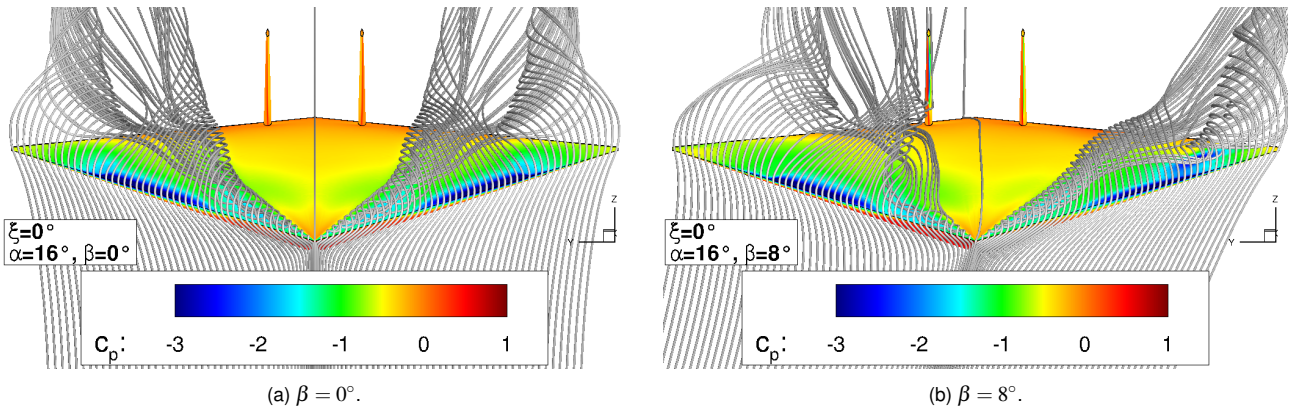


Figure 12: Field streamlines of the clean wing configuration at  $\alpha = 16^\circ$ .



the gradient change, Figure 10b. In relation the W/T data, the change of the  $C_{mx}$  values computed by CFD is much more distinctive.

## 4.2 Configuration With Deflected M/B Flaps

### 4.2.1 Longitudinal Motion

In the following, the SAGITTA diamond wing demonstrator configuration is considered with deflected M/B flaps. Figure 14 depicts the complete set of the aerodynamic coefficients, which are shown in dependence of the angle of attack  $\alpha$  and the M/B flap deflection angle  $\xi$ . The contour plots exclusively present the results of the CFD computations without sideslip angle,  $\beta = 0^\circ$ . The longitudinal aerodynamic coefficients  $C_D$ ,  $C_L$  and  $C_{my}$ , Figure 14a to Figure 14c, show the expected and desired characteristics. Due to the increased pressure drag at the M/B control devices, which is associated with the surface streamline pattern indicated in Figure 15, the drag coefficient  $C_D$  is found to be increased for the configurations with deflected M/B flaps. With respect to the M/B flap deflection angle, a complete symmetrical contour plot is observed. Due to the longitudinal motion, this also holds for the other two longitudinal aerodynamic

coefficients, the lift coefficient  $C_L$  and the pitching moment coefficient  $C_{my}$ . Moreover, they vary only slightly with varying M/B flap deflection angle, even at higher angles of attack. Following, no relevant non-linearities are observed.

In Figure 14d to Figure 14f, the aerodynamic coefficients associated with the lateral motion are presented. Based on the longitudinal flight condition without sideslip angle, the plots indicate the available roll control effectiveness and the associated coupling effects to initiate a roll maneuver.

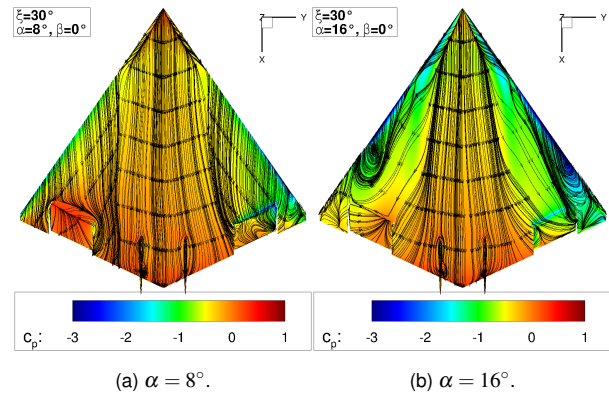


Figure 15: Surface streamlines of the configuration with deflected M/B flaps ( $\xi = 30^\circ$ ) at  $\beta = 0^\circ$ .

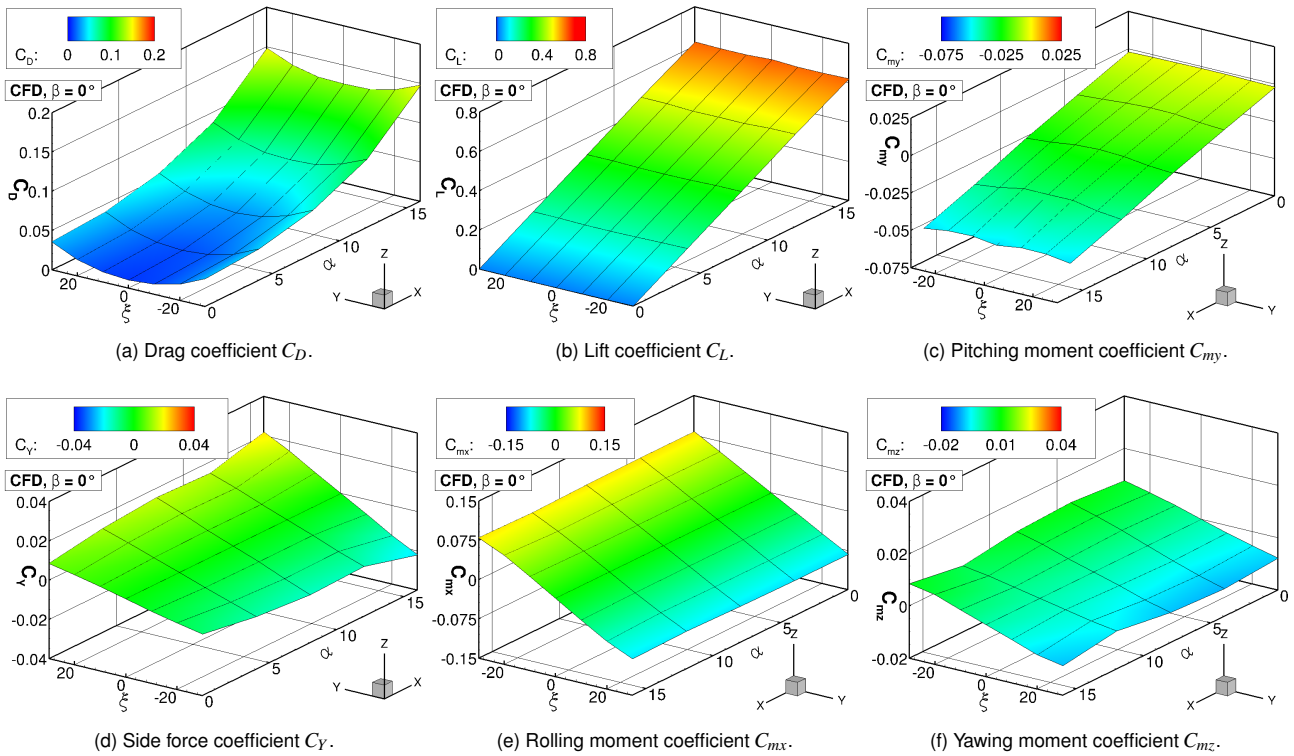


Figure 14: Aerodynamic coefficients versus of angle of attack  $\alpha$  and M/B flap deflection  $\xi$  at  $\beta = 0^\circ$ .



For positive flap deflection angles  $\xi$  (right M/B flap down, left M/B flap up), negative rolling moment coefficients are observed over the whole angle of attack regime and vice versa, Figure 14e. In comparison to the  $C_{mx}$  values generated by the clean wing configuration with present sideslip angle (Figure 10b), the maximum achievable rolling moment coefficients are now considerably larger. The roll control effectiveness does not change significantly with increasing angle of attack, as the wing tip separation region does not influence the M/B flap up to  $\alpha = 16^\circ$ . At this angle of attack, the flow over the M/B flap is dominated by the inboard leading-edge vortex, which passes the wing surface in chord-wise direction, Figure 15b. The other two aerodynamic coefficients, namely  $C_Y$  and  $C_{m_z}$ , indicate the coupling effects associated with the deflected M/B flaps. Some roll-yaw coupling is observed, Figure 14f. Compared to the maximum rolling moment coefficient achievable ( $C_{mx,Max} \approx \pm 0.075$ ), the maximum yawing moment coefficients originating from the M/B flap deflection result in  $C_{m_z,Max} \approx \pm 0.01$ , which roughly corresponds to a factor of  $1/7$ . With increasing angle of attack, weak non-linearities are noticed. This trend also holds for the side force coefficient  $C_Y$ , Figure 14d. The gradient with respect to  $\xi$  in-

creases at higher angles of attack, leading as well to increased maximum side force coefficients.

#### 4.2.2 Lateral Motion

Next, the set of aerodynamic coefficients is presented for the lateral motion with a sideslip angle of  $\beta = 8^\circ$ , Figure 16. In comparison to the latter case without sideslip angle, the CFD computations now result in more varying contour plots, which is caused by the different flow characteristics on both wing half surfaces. In order to discuss the relevant flow phenomena, Figure 17 is introduced, which depicts the flow field for selected flight conditions with deflected M/B flaps and present sideslip angle. At first, the aerodynamic coefficients associated with the longitudinal motion are regarded, Figure 16a to Figure 16c. With increasing angle of attack, the drag and the lift coefficient  $C_D$  and  $C_L$  are slightly increased for negative M/B flap deflection angles compared to positive  $\xi$  values. This is mainly caused by the different trajectories of the leeward inboard and outboard leading-edge vortices and the size of the windward separation region, Figure 17, which occur due to positive and negative M/B flap deflections. For the pitching moment coefficient  $C_{m_y}$ , the dependency is much more distinctive, and the non-linearities

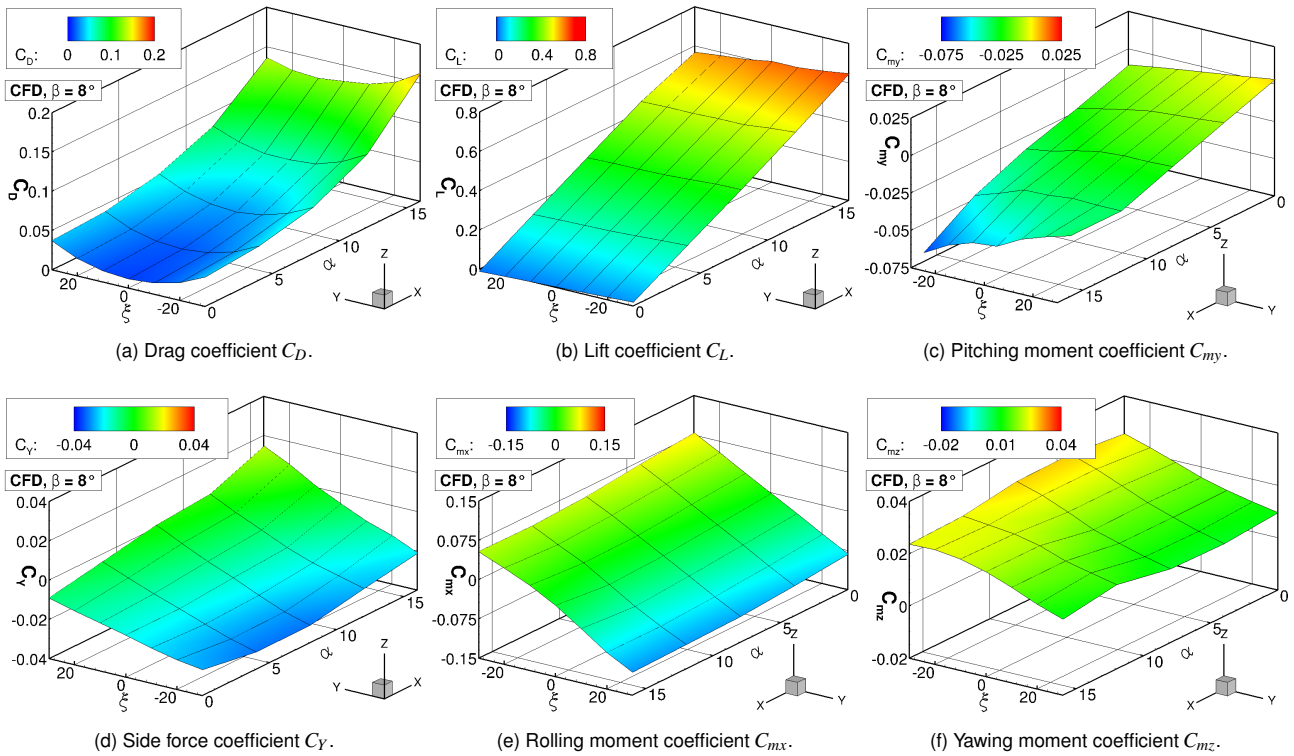


Figure 16: Aerodynamic coefficients versus angle of attack  $\alpha$  and M/B flap deflection  $\xi$  at  $\beta = 8^\circ$ .

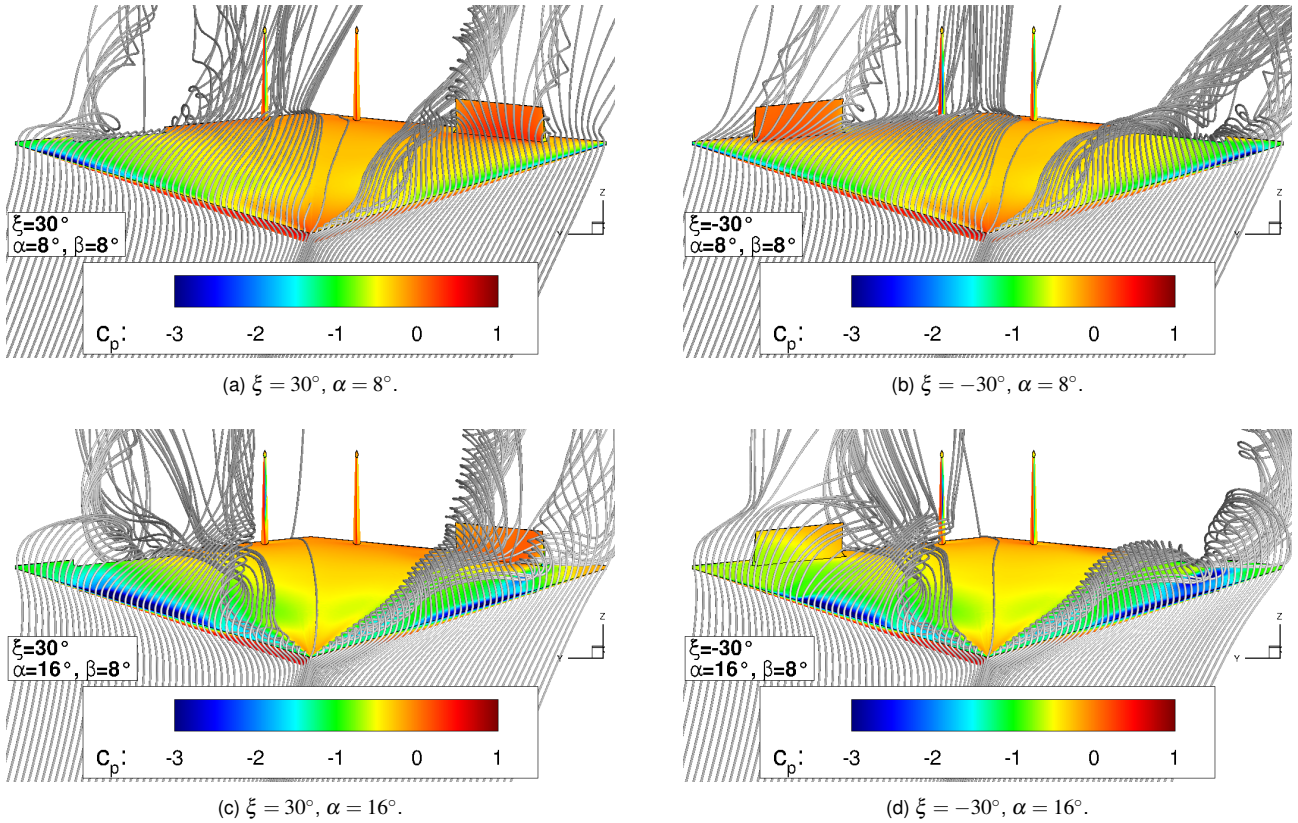


Figure 17: Field streamlines of the configuration with deflected M/B flaps ( $\xi = \pm 30^\circ$ ) at  $\beta = 8^\circ$ .

increase considerably at higher angles of attack, Figure 14c and Figure 16c. Especially for  $\alpha = 16^\circ$  and  $\xi = \pm 30^\circ$ , the pitching moment coefficient is significantly changed.

The lateral aerodynamic coefficients  $C_Y$ ,  $C_{mx}$  and  $C_{mz}$  are influenced more considerably by the sideslip angle of  $\beta = 8^\circ$ , Figure 16d to Figure 16f. With increasing angle of attack, the roll control effectiveness slightly decreases for

negative M/B flap deflection angles, Figure 16e, since the wing tip separation region on the windward side dominates the flow field on the right M/B flap to a greater extent. At the angle of attack of  $\alpha = 16^\circ$ , flow reversal occurs on the entire M/B flap of the right wing half, Figure 18a. For positive  $\xi$  values, in contrast, the roll control effectiveness increases, as it can be noticed from Figure 16e. The wing tip separation region on the windward side is in this case considerably smaller, and the flow field of the right M/B flap is not as much influenced by the flow reversal, Figure 18b. The variations of the rolling moment coefficient with increasing angle of attack, however, do not result in distinct non-linearities of the  $C_{mx}$  values, as the size of the wing tip separation region changes continuously with varying free stream parameters  $\alpha$  and  $\beta$  and the M/B flap deflection angle.

As it can be expected, the side force and the yawing moment coefficient  $C_Y$  and  $C_{mz}$  are affected as well. The absolute levels of the contour plots change considerably, which is mainly caused by the effects of the double V/T as discussed for the clean wing configuration. If one compares the different levels (Figures 14d, 14f, and Figures 16d, 16f, respectively), the variations are in the same magnitude as

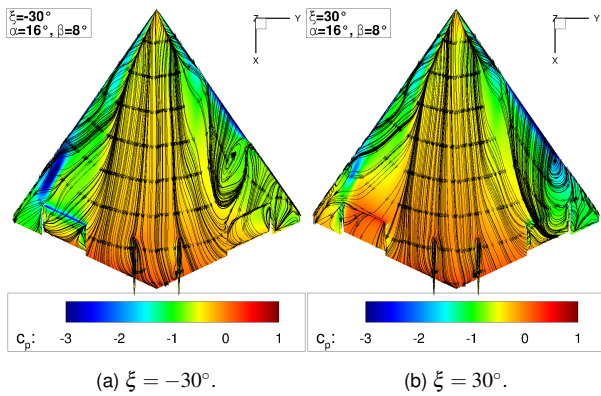


Figure 18: Surface streamlines of the configuration with deflected M/B flaps ( $\xi = \pm 30^\circ$ ) at  $\alpha = 16^\circ$  and  $\beta = 8^\circ$ .

the absolute values presented for the clean wing configuration in Figure 10a and Figure 10c. The additional coupling effects originating from the M/B flaps are discussed in the following paragraph, Section 4.2.3.

#### 4.2.3 M/B Flap Efficiency

Finally, the M/B flap efficiency is analyzed, Figure 19. The derivatives of the lateral aerodynamic coefficients are built with respect to the M/B flap deflection angle  $\xi$  by linear interpolation around the discrete data points. The resulting values of the CFD computations are shown for both sideslip angles discussed in the previous sections ( $\beta = 0^\circ$  and  $\beta = 8^\circ$ ). The most important derivative in this analysis, namely  $\frac{dC_{mx}}{d\xi}$ , is defined as the M/B flap efficiency factor. For the longitudinal motion, it results in a contour plane with only slightly varying values over the angle of attack and M/B flap deflection angle regime, Figure 19b. This observation confirms the results of Section 4.2, in which the available roll control effectiveness with increasing angle of attack is discussed. At  $\alpha = 16^\circ$ , the derivative slightly decreases in its absolute value for deflected M/B flaps, which reduces the M/B flap efficiency. This effect is intensified in the lateral motion with present sideslip angle, Figure 19e. The non-

linearities in the contour plane of the M/B flap efficiency factor increase, especially at  $\alpha = 12^\circ$  and  $\alpha = 16^\circ$ . For a more detailed discussion, Figure 20 is additionally introduced. Both the CFD and the W/T data sets of the M/B flap efficiency factor are presented for selected flight conditions. Overall, the agreement between the results of both data sources is satisfactorily, as the derivatives are predicted similar to each other. Compared to the W/T experiments, the M/B flap efficiency factor of the CFD computations is in general slightly larger. At zero angle of attack, Figure 20a and Figure 20b, the derivative is constant for all M/B flap deflections and does not change with sideslip angle either. The absolute values of the M/B flap efficiency factor are close to each other. At  $\alpha = 16^\circ$ , in contrast, the nonlinearities already discussed become more obvious, Figure 20c and Figure 20d. At the angle of attack of  $\alpha = 16^\circ$  and without sideslip angle, the M/B flap efficiency factor decreases symmetrically in its absolute value with deflected M/B flaps. For the flight condition at  $\alpha = 16^\circ$  and  $\beta = 8^\circ$ , the maximum value of the M/B flap efficiency factor is observed at  $\xi = 10^\circ$ . Moreover, it is larger in its absolute value compared to the maximum value of the longitudinal motion.

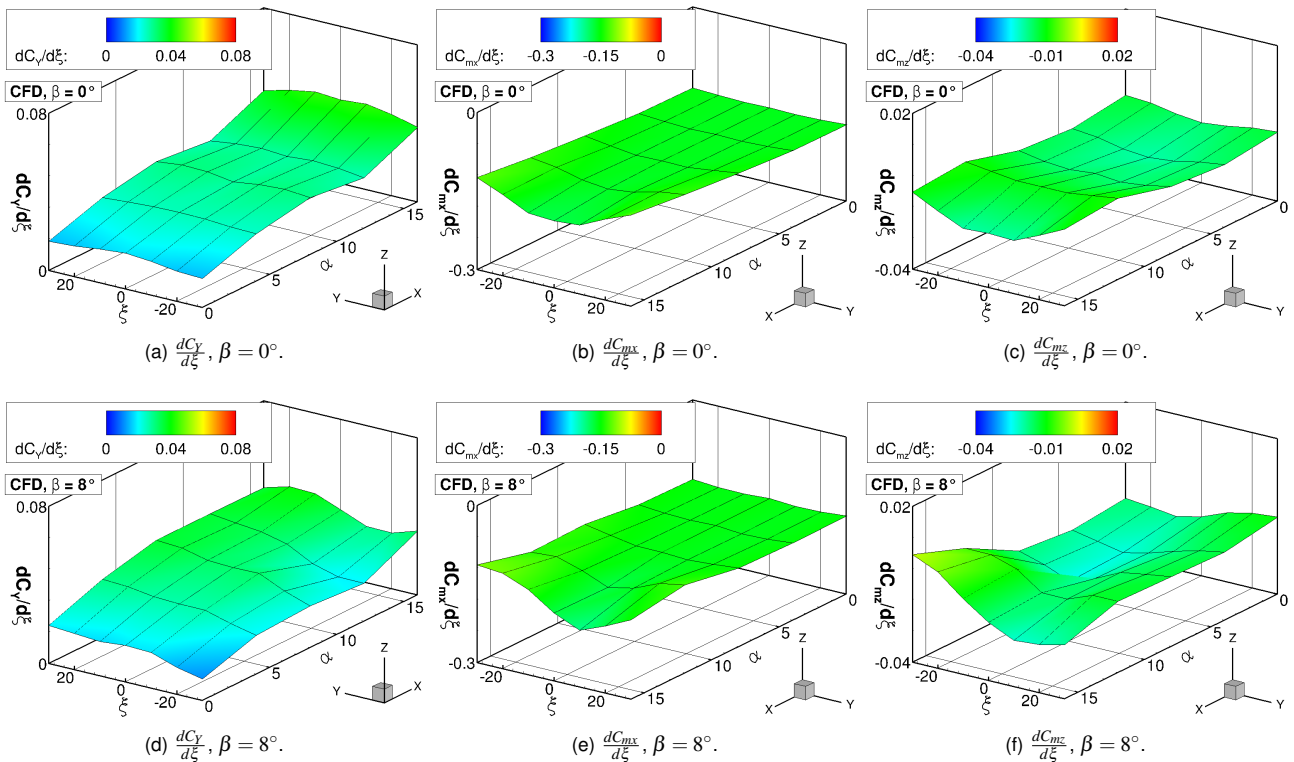


Figure 19: Aerodynamic derivatives versus angle of attack  $\alpha$  and M/B flap deflection  $\xi$  at  $\beta = 0^\circ$  and  $\beta = 8^\circ$ .

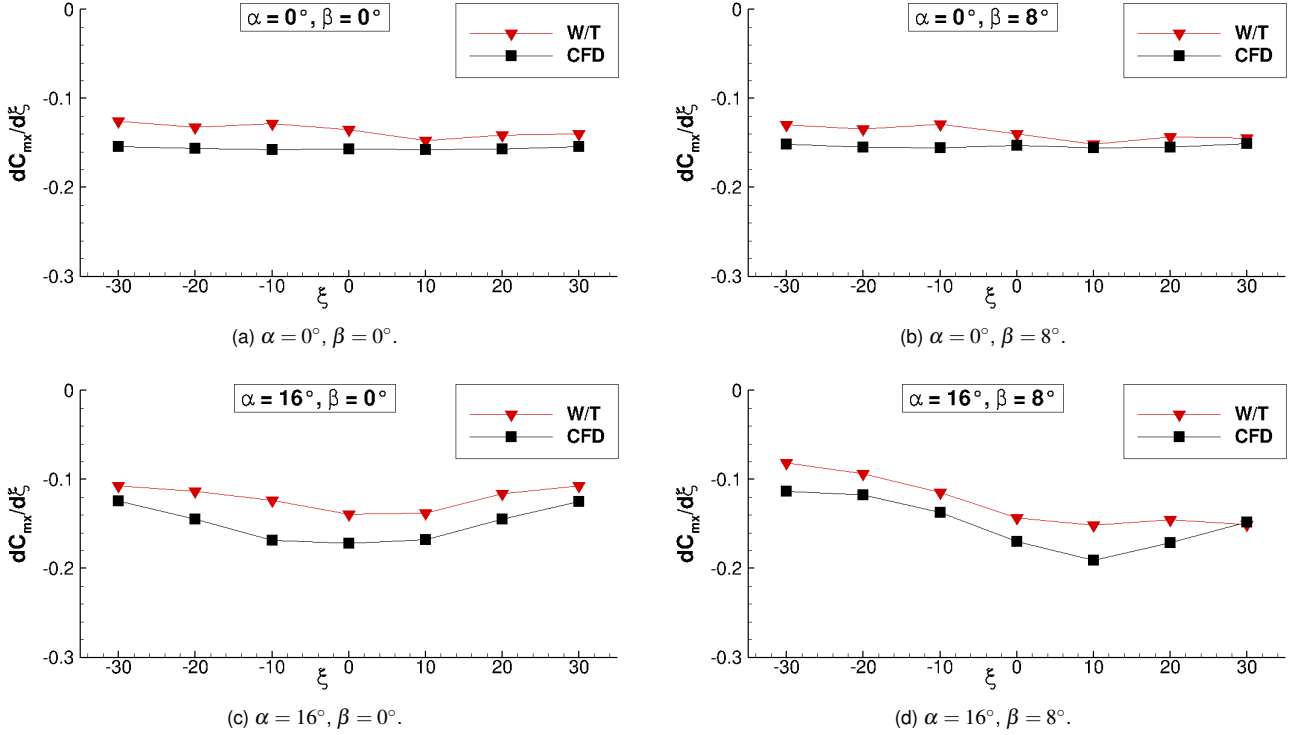


Figure 20: M/B flap efficiency factor  $\frac{dC_{mx}}{d\xi}$  for selected flight conditions.

The side force and the yawing moment derivative  $\frac{dC_y}{d\xi}$  and  $\frac{dC_{mz}}{d\xi}$  show, even in the longitudinal motion, weak non-linearities with respect to the angle of attack, Figure 19a and Figure 19c. The overall values, however, are considerably smaller than the values of the M/B flap efficiency factor. With present sideslip angle, additional non-linearities with respect to the M/B flap deflection angle become obvious, Figure 19d and Figure 19f. These coupling effects arise due to the deflected M/B flaps and act in addition to them introduced by the double V/T as discussed above.

## 5 CONCLUSION AND OUTLOOK

Numerical investigations on the SAGITTA diamond wing demonstrator configuration have been presented and discussed in the present article. In order to examine the validity of the steady-state RANS computations, the numerical results have been compared to existing W/T data sets. It turns out that the overall agreement of the CFD and W/T results is satisfactorily. Certain deviations are observed, which can however be attributed to different conditions of the boundary layer characteristics. The CFD computations have been run fully turbulent, whereas the flow in the experimental investi-

gations has not been tripped, leading to natural transition at the W/T model.

In addition to the analysis of the clean wing configuration, the configuration with deflected M/B flaps has been considered. Numerous CFD computations have been conducted, which vary in the angle of attack, the sideslip angle and the M/B flap deflection angle. In particular, the flow phenomena occurring on the diamond wing configuration, the associated aerodynamic coefficients and the M/B flap efficiency have been analyzed and evaluated. For the longitudinal motion, the roll control effectiveness due to deflected M/B flaps to initiate a roll maneuver is mostly maintained with increasing angle of attack. The M/B flaps show an almost constant flap efficiency factor  $\frac{dC_{mx}}{d\xi}$ . At  $\alpha = 16^\circ$ , it is slightly reduced with increasing M/B flap deflection. The coupling effects with respect to the side force and the yawing moment coefficient are small. For the lateral motion with present sideslip angle, however, the non-linearities in the aerodynamic coefficients increase with increasing angle of attack, which is caused by different flow field characteristics on both wing half surfaces. On the windward side, the inboard leading-edge vortex extenuates, while the wing tip separation region with irregular flow grows in size. On the leeward side, in contrast, the inboard leading-edge vortex is strengthened

and an outboard leading-edge vortex emerges due to the increased effective wing sweep. This influences the entire set of aerodynamic coefficients and their derivatives. For positive sideslip angles, the M/B flap efficiency factor  $\frac{dC_{mx}}{d\xi}$  is increased in its absolute value for positive M/B flap deflections and decreased for negative  $\xi$  values.

Overall, the present analysis provides valuable add on information for the aerodynamic data module (ADM) within the SAGITTA demonstrator program. Supplementary to the existing W/T data sets, which comprise only force and moment data, the numerical investigations have set up a second, broad data base with additional information about the flow field. Thereby, the CFD results allow for a more detailed flow field analysis of the occurring flow phenomena, which is essential for the assessment and discussion of the aerodynamic characteristics of the SAGITTA diamond wing demonstrator configuration.

In order to enlarge the numerical data sets even further, additional CFD computations for the other control devices are of high interest. Especially the flow phenomena associated with the deflected vortex flaps at the wing tip are to be investigated, as the W/T experiments have shown non-linear effects with increasing angle of attack and sideslip angle.

## ACKNOWLEDGEMENTS

The support of this investigation by Airbus Defence and Space within the SAGITTA demonstrator program is gratefully acknowledged. Furthermore, the authors thank the German Aerospace Center (DLR) for providing the DLR TAU-Code used for the numerical investigations. The support of CENTAURSoft for its guidance during the mesh generation process is also highly appreciated. Moreover, the authors gratefully acknowledge the Gauss Centre for Supercomputing e.V. ([www.gauss-centre.eu](http://www.gauss-centre.eu)) for funding this project by providing computing time on the GCS Supercomputer SuperMUC at Leibniz Supercomputing Centre (LRZ, [www.lrz.de](http://www.lrz.de)).

## REFERENCES

- [1] Schütte, A., Einarsson, G., Raichle, A., Schöning, B., and Mönnich, W., "Numerical Simulation of Maneuvering Aircraft by Aerodynamic, Flight-Mechanics, and Structural-Mechanics Coupling," *Journal of Aircraft*, Vol. 46, No. 1, 2009, pp. 53–64.
- [2] Schütte, A., Hummel, D., and Hitzel, S. M., "Flow Physics Analyses of a Generic Unmanned Combat Aerial Vehicle Configuration," *Journal of Aircraft*, Vol. 49, No. 6, 2012, pp. 1638–1651.
- [3] Colgren, R. and Loschke, R., "Effective Design of Highly Maneuverable Tailless Aircraft," *Journal of Aircraft*, Vol. 45, No. 4, 2008, pp. 1441–1449.
- [4] Stenfelt, G. and Ringertz, U., "Lateral Stability and Control of a Tailless Aircraft Configuration," *Journal of Aircraft*, Vol. 46, No. 6, 2009, pp. 2161–2164.
- [5] Schütte, A., Huber, K., and Boelens, O., "Static and Dynamic Numerical Simulations of a Generic UCAV Configuration With and Without Control Devices," *32<sup>nd</sup> AIAA Applied Aerodynamics Conference, Atlanta (GA), United States, June 16–20, 2014*, No. 2132 in AIAA 2014.
- [6] Seifert, J., "SAGITTA - Nationale Forschungs Kooperation für fortschrittliche UAV-Technologien im Rahmen der Open Innovation Initiative von Cassidian," *61<sup>st</sup> Deutscher Luft- und Raumfahrtkongress, Berlin, Germany, September 10–12, 2012*, No. 1352 in DLRK 2012.
- [7] Hövelmann, A. and Breitsamter, C., "Aerodynamic Characteristics of the SAGITTA Diamond Wing Demonstrator Configuration," *61<sup>st</sup> Deutscher Luft- und Raumfahrtkongress, Berlin, Germany, September 10–12, 2012*, No. 1220 in DLRK 2012.
- [8] Geiser, M. and Heller, M., "Flight Dynamics Analysis and Basic Stabilization Study in Early Design Stages of the SAGITTA Demonstrator UAV," *61<sup>st</sup> Deutscher Luft- und Raumfahrtkongress, Berlin, Germany, September 10–12, 2012*, No. 1329 in DLRK 2012.
- [9] Özger, E., "Aerodynamic Model Validation of Unmanned Research Demonstrator SAGITTA," *61<sup>st</sup> Deutscher Luft- und Raumfahrtkongress, Berlin, Germany, September 10–12, 2012*, No. 1253 in DLRK 2012.
- [10] Hövelmann, A. and Breitsamter, C., "Leading-Edge Geometry Effects on the Vortex System Formation of a



- Diamond Wing Configuration,” 31<sup>st</sup> AIAA Applied Aerodynamics Conference, San Diego (CA), United States, June 24–27, 2013, No. 3187 in AIAA 2013.
- [11] Gerhold, T., “Overview of the Hybrid RANS Code TAU,” *MEGAFLOW - Numerical Flow Simulation for Aircraft Design*, Vol. 89 of Notes on Numerical Fluid Mechanics and Multidisciplinary Design, Springer Verlag, 2005, pp. 81–92.
- [12] Schwamborn, D., Gerhold, T., and Heinrich, R., “The DLR TAU-Code: Recent Applications in Research and Industry,” 4<sup>th</sup> European Conference on Computational Fluid Dynamics (ECCOMAS CFD 2006), Egmond aan Zee, The Netherlands, September 5–8, 2006.
- [13] Fritz, W., Davis, M. B., Karman, S. L., and Michal, T., “Reynolds-Averaged Navier–Stokes Solutions for the CAWAPI F-16XL Using Different Hybrid Grids,” *Journal of Aircraft*, Vol. 46, No. 2, 2009, pp. 409–422.
- [14] Schütte, A., Boelens, O. J., Oehlke, M., Jirásek, A., and Löser, T., “Prediction of the Flow Around the X-31 Aircraft Using Three Different CFD Methods,” *Aerospace Science and Technology*, Vol. 20, No. 1, 2012, pp. 21–37.
- [15] Schütte, A. and Lüdeke, H., “Numerical Investigations on the VFE-2 65-Degree Rounded Leading Edge Delta Wing Using the Unstructured DLR TAU-Code,” *Aerospace Science and Technology*, Vol. 24, No. 1, 2013, pp. 56–65.
- [16] Jameson, A., Schmidt, W., and Turkel, E., “Numerical Solutions of the Euler Equations by Finite Volume Methods Using Runge-Kutta Time-Stepping Schemes,” 14<sup>th</sup> AIAA Fluid and Plasma Dynamics Conference, Palo Alto (CA), United States, June 23–25, 1981, No. 1259 in AIAA 1981.
- [17] Turkel, E., “Improving the Accuracy of Central Difference Schemes,” *NASA CR 181712*, 1988.
- [18] Jameson, A. and Yoon, S., “Lower-Upper Implicit Schemes with Multiple Grids for the Euler Equations,” *AIAA Journal*, Vol. 25, No. 7, 1987, pp. 929–935.
- [19] Jameson, A. and Yoon, S., “Multigrid Solution of the Euler Equations Using Implicit Schemes,” *AIAA Journal*, Vol. 24, No. 11, 1986, pp. 1737–1743.
- [20] Spalart, P. R. and Allmaras, S. R., “One-Equation Turbulence Model for Aerodynamic Flow,” 30<sup>th</sup> AIAA Aerospace Sciences Meeting & Exhibit, Reno (NV), United States, January 6–9, 1992, No. 439 in AIAA 1992.
- [21] Allmaras, S. R., Johnson, F. T., and Spalart, P. R., “Modifications and Clarifications for the Implementation of the Spalart-Allmaras Turbulence Model,” 7<sup>th</sup> International Conference on Computational Fluid Dynamics (ICCFD7), Big Island (HI), United States, July 9–13, 2012.